Optical Nanoantennas for Tip-Enhanced Raman Spectroscopy

Thiago L. Vasconcelos, Bráulio S. Archanjo, Bruno S. Oliveira, William F. Silva, Rafael S. Alencar, Cassiano Rabelo, Carlos A. Achete, Ado Jorio, and Luiz Gustavo Cançado

(Invited Paper)

***Abstract*—The role of plasmon resonance on the optical efficiency of nanoantennas for tip-enhanced Raman spectroscopy (TERS) is reviewed. Technical details on surface plasmon polaritons (SPP), localized surface plasmon resonance (LSPR), and the plasmon gap mode are provided. Nanotechnology engineering is necessary to adequate the nanoantenna's size, shape and composition to match resonance conditions with the exciting radiation source. Computational simulation guides the development of new types of plasmonic nanoantennas with different materials and morphologies, specially designed to reach target applications. An overview on a recently developed nanoantenna composed by a truncated micropyramidal body with a nanopyramid end is presented. The characteristic length *L* of the nanopyramid tip is dimensioned to fine-tune LSPR modes, giving rise to the so-called plasmon-tunable tip pyramid (PTTP). The plasmonic properties of this type of probe were investigated by electron energy loss spectroscopy and computational simulations, reveling that PTTPs act as monopole nanoantennas. TERS results obtained with the PTTPs demonstrate the achievement of unprecedent levels of field enhancement mediated by LSPR with excellent reproducibility rate.**

***Index Terms*—Optical nanoantennas, tip-enhanced Raman spectroscopy, plasmon resonance, LSPR, HIM, graphene, nanopattern.**

I. Introduction

OPTICAL nanoantennas are metallic structures specifically designed to support dipole [1]–[3] or monopole [4], [5] localized surface plasmon resonance (LSPR) modes driven by radiation fields with specific wavelengths (λ_{ligth}). As for any ordinary antenna, they are meant to convert propagating far-field into localized near-field energy/information, and vice-versa. Many applications benefit from the tunability of the LSPR's discrete energy modes, which is operated by adjusting the nanoantenna shape and size [6], [7]. Examples can be found in contrast agents for bio-imaging [8], colors devices [9], biosensing devices [10] and cancer cell imaging and photothermal therapy [11].

Tip-enhanced Raman spectroscopy (TERS) is a type of scanning near-field optical microscopy (SNOM) specially adapted to the vast field of Raman spectroscopy [12]–[17]. As for any SNOM technique, the nanoantennas are firstly employed for local illumination [12], [18]. The incident radiation field interacts with the material system, and the product of this interaction gives rise to inelastically scattered radiation fields (the frequencies are distinct from the incident field). The scattered fields contain valuable local chemical and structural spectral information on the material's properties. The nanoantenna is responsible for collecting near-field components of the scattered radiation fields, transposing them into propagating radiation that reaches a detector device located in the far-field range. By employing the SNOM schema, TERS carries the advantage (over usual Raman spectroscopy) to perform chemical and structural analyses with spatial resolution ranging from tens to tenth of nanometers [18]–[21]. The main drawback is the intrinsically low yield of Raman scattering: TERS has to deal with extremely weak fields, originated from tiny areas. The near-field information coming from the probed area ($\leq$100 nm^2) competes with the far-field signal coming from the whole focus area ($\geq$60,000 nm^2). For this reason, a crucial quality factor in the TERS technology is the optical efficiency of the nanoatenna, which must be sufficiently high to guarantee optical contrast between near-field and far-field signals.

To achieve this degree of quality, the nanoantenna should support LSPR modes tuned to the incident laser used in the TERS measurement. For radio and microwave antennas, the matching occurs when the antenna's characteristic length (L) is an even multiple of $\lambda_{\mathrm{ligth}}/2$. However, within the visible spectral range, metals are no longer perfect conductors, and the surface plasmon's effective wavelength (λ_{eff}) becomes considerably different from the wavelength of the light in free-space, with

Manuscript received April 28, 2020; revised June 25, 2020; accepted July 7, 2020. Date of publication July 10, 2020; date of current version August 18, 2020. This work was supported by Inmetro, CNPq under Grants 309537/2019-3, 429165/2018-8, 302775/2018-8, 305881/2019-1, and 436381/2018-4, in part by FINEP under Grants 01.13.0330.00 and 01.13.0357.00, in part by SisNANO, MCTI Sibratec-Nano, INCT Nanomateriais de Carbono, CAPES-PROBRAL under Grants 88881.198744/2018-01, in part by FAPEMIG under Grant APQ-01361-14, and in part by FAPERJ. *(Corresponding author: Thiago Vasconcelos.)*

Thiago L. Vasconcelos, Bráulio S. Archanjo, Bruno S. Oliveira, William F. Silva, and Carlos A. Achete are with the Divisão de Metrologia de Materiais, Instituto Nacional de Metrologia, Qualidade e Tecnologia (Inmetro), Duque de Caxias 25250-020, Brazil (e-mail: tlvasconcelos@inmetro.gov.br; bsarchanjo@inmetro.gov.br; bsoliveira-prometro@Inmetro.gov.br; williamsilvakse@gmail.com; caachete@inmetro.gov.br).

Rafael S. Alencar is with the Faculdade de Física, Universidade Federal do Pará, Belém 66075-110, Brazil (e-mail: rsalencar@ufpa.br).

Cassiano Rabelo, Ado Jorio, and Luiz Gustavo Cançado are with the Departamento de Física, Universidade Federal de Minas Gerais, Belo Horizonte 30270-901, Brazil (e-mail: cassianorabelo@ufmg.br; adojorio@fisica.ufmg.br; cancado@fisica.ufmg.br).

Color versions of one or more of the figures in this article are available online at https://ieeexplore.ieee.org.

Digital Object Identifier 10.1109/JSTQE.2020.3008526

$\lambda_{\text{eff}} < \lambda_{\text{ligth}}$ [12]. Therefore, proper nanoantenna engineering is necessary to adequate the nanoantenna's size, shape and composition to the wavelength of the incident laser light used in the TERS experiment.

This manuscript presents an overall description of the rules of surface plasmon resonances in different types of optical nanoantennas used in TERS systems, approaching several technical aspects such as modeling, engineering and characterization. The recent creation of monopole TERS nanoantennas fabricated thorough a high reproducible lithography process is revisited. This monopole-type nanoantenna, denominated as plasmon-tunnable tip pyramid (PTTP), is able to achieve extremely high levels of field enhancements with spatial resolution beyond 20 nm. To illustrate the potential of the PTTPs as special probes for TERS, near-field Raman images and analysis of 2D materials are presented.

II. Definitions of Optical Efficiency

There are several distinct ways to define and measure the optical efficiency of a TERS probe. The most primary one is the spectral signal enhancement, F_{TERS}[14], also referred as contrast [22], defined as the ratio between the Raman intensities measured in the presence ($I_{\text{tip-down}}$) and without the presence ($I_{\text{tip-up}}$) of the TERS probe. Because the former contains contributions from both near-field (NF) and far-field (FF) signals, F_{TERS} is written on the form:

$$F_{\text{TERS}} = \frac{I_{\text{tip-down}}}{I_{\text{tip-up}}} = \frac{I_{\text{FF}} + I_{\text{NF}}}{I_{\text{FF}}}. \tag{1}$$

However, this quantity cannot be intrinsically addressed to the probe because it also depends on the sample dimension, becoming smaller as the sample's dimension gets higher. For example, the same probe provides lager F_{TERS} considering the TERS signal from a carbon nanotube (1D) than from a graphene (2D), simply because the FF signal originates from the whole focus area in the graphene case, boosting up I_{FF}. To address this problem, a most accurate definition should take into account the area of the sample's surface illuminated by the incident laser field, defined here as A_{FF}, and also the area under the nanoantenna's apex, A_{NF}. This type of optical efficiency, known as signal enhancement factor, M_{TERS}, is defined on the form:

$$M_{\text{TERS}} = (F_{\text{TERS}} - 1)\frac{A_{\text{FF}}}{A_{\text{NF}}}. \tag{2}$$

Recently, a more robust way to measure the optical efficiency of TERS probes was introduced. The method takes into account the evolution of the TERS intensity as the nanoantenna (tip) approaches the sample's surface [23]–[25]. The measured TERS intensity is plotted as a function of the tip-sample distance, giving rise to the so-called tip-approach curve [26]. The field enhancement factor f_{e}, which scales with $M_{\text{TERS}}^{1/4}$, can be extracted from the fitting of the approach curves trough theoretical functions that take into account geometrical factors (e.g. sample's dimensionality, nanoantenna apex's radius), material properties (e.g. symmetry of vibrational modes and respective Raman tensors, correlation length of optical phonons), electromagnetic interactions between the incident or scattered fields and the nanoantenna (antenna's polarizability), and filed-field interactions giving rise to interference effects that resemble the coherernce properties of the scattered fields and the material system [23], [24], [27].

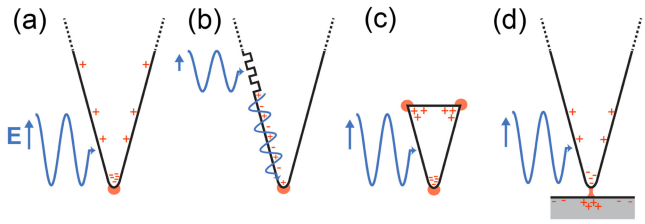

Fig. 1. Conceptual illustrations of different types of mechanisms for electric field enhancement at the apex of a sharp metallic tip. (a) Lightning-rod effect (LRE). (b) Surface plasmon polariton (SPP). (c) Localized surface plasmon resonance (LSPR). (d) Gap plasmon mode.

III. Enhancement Mechanisms

The first probe reported in the literature used in a SNOM experiment was a tapered optical fiber coated with a metallic film containing an aperture on its apex [28]. The aperture was used for both emission and collection of incident and scattered radiation, respectively [29]. The metallic coating was responsible for generating enhancement of local fields. The sample's surface was raster scanned by the aperture, and the intensity of the collected light was used to construct 2D images with lateral resolution defined by the size of the aperture (∼50 nm) [12]. The main disadvantage of this approach is the low optical efficiency, which drastically drops as the aperture size becomes smaller. Besides, the metallic coating is extremely sensitive to laser heating, and low optical input is mandatory. All together, it becomes clear that optical efficiency competes with spatial resolution in experiments using aperture probes. Since TERS requires both, this is not a good approach for TERS. It was not accidentally that the first TERS experiments reported in the literature were performed using solid (apertureless) metallic tips as nanoatennas [30], [31]. Nowadays, there are dozens of different designs of apertureless probes for TERS [18]. In the following, we summarize the main known enhancement mechanisms that can improve their optical efficiencies.

A. Lightning Rod Effect

The non-resonant lightning rod effect (LRE) is a mechanism that generates an enhanced electric field localized at the apex of an illuminated sharp tapered metallic tip [12], [15], [32]. The source of this secondary field is a high-local surface charge density driven by the external electromagnetic radiation field. The effect is stronger if the external field is polarized parallel to the tip's shaft [12], [32], [33]. Besides, polarization-dependent spectral signal enhancement can be used to revel crystal domains and ordered organic nanostructures [34].

For instance, a smooth, semi-infinite conical gold tip, such as the one depicted in Fig. 1(a), is not able to support any type of plasmon resonance. In such featureless probes, the only possible mechanism of local electric field enhancement is the LRE. A clear example that shows that LRE does not involve any type of plasmon resonance is the occurrence of local electric field enhancement in tungsten conical tips at optical frequencies [32],

[35], [36]. Surface plasmons are forbidden in tungsten within this frequency range, being limited to the near-infrared range. However, since the plasma frequency occurs at the UV range, non-resonant surface electron oscillations are allowed. Therefore, the local field enhancement can only be due to LRE.

Because LRE is essentially non-resonant, the associated optical efficiency depends primarily on the probe's morphology and electrical conductivity at the frequency of the radiation field that drives the surface charge density [18]. The main geometrical factors are the conical open semi-angle (α) and apex size (ϕ). The optical efficiency increases as ϕ decreases and, for gold tips with $\phi \sim 15$ nm, $\alpha \sim 35^{\circ}$ provides the optimal condition [32]. In terms of materials properties, the dielectric function ε plays the most important role. Small imaginary components of ε leads to better enhancement. In general, LRE provides moderate spectral signal enhancement. For TERS experiments performed in graphene, the best values reported in the literature indicate $F_{\mathrm{TERS}} \sim 3$ and $M_{\mathrm{TERS}} \sim 460$ [5], [24], [37].

B. Surface Plasmon Polariton

Surface plasmon polariton (SPP) is an electromagnetic excitation that propagates over the surface of a metal through a longitudinal wave of conduction electrons [38]. It can be obtained analytically from the solution of the Helmholtz's wave equation applied to a metal/dielectric interface. At low frequency range - radio to microwave - SPP can be directly excited by electromegnetic radiation because, in this range, $\lambda_{\mathrm{ligth}} \approx \lambda_{\mathrm{eff}}$. This condition does not stand for near-infrared and visible. Photon-plasmon coupling is forbidden within this spectral range because the photon's associated momentum is considerable smaller than the plasmon's momentum. A common way to overcome this problem is to provide extra momentum to the system by drawing a one-dimensional grating at the metal surface, as shown in Fig. 1(b). The periodicity of the grating can be designed to provide the right condition for momentum conservation.

Ropers *et al.* showed that the formation of SPP can be mediated by the presence of a grating-coupler (milled by focused ion beam, FIB) on the smooth surface of a gold tip's shaft, located $10\,\mu$m away from its apex [39]. Berweger S. *et al.* successfully applied this type of probe to perform TERS on a malachite green sample [40]. Due to the geometrical constraints needed to couple the incident light with the SPP, this schema requires two objective lenses: one to illuminate the tip at an specific angle of incidence, and the other to collect the generated TERS signal. The advantage of such a schema is the acquisition of a clean NF spectrum, since no FF signal is collected by the second objective lens. The most critical aspect is the surface smoothness of the taper gold tip along the $10\,\mu$m portion adjacent to its apex. Starting from the milled grating, the SPP propagates through this length, and any defect along the way can generate damping or scattering, compromising the optical efficiency.

C. Localized Surface Plasmon Resonance

When electromagnetic radiation is focused on a metallic nanostructure with subwavelength dimensions, the excited electron surface plasma undergoes a collective coherent oscillation that polarizes the nanostructure with the same frequency as the incident light [41]. This is schematically illustrated in Fig. 1(c) for an elongated tip with dipolar polarization. This process is resonant at a particular set of frequencies known as electric dipole or monopole resonance modes, which give rise to the well-known bright intense colors of metal nanoparticles - described here as resonant optical nanoantennas [6], [9], [41]. This phenomenon is termed localized surface plasmon resonance. The main attribute of this type of schema is that the wavelength of the resonant plasmon modes can be tuned by changing the nanoantenna shape and size. As in classical example, the wavelength of the first LSPR dipolar mode – LSPR$^{(1)}$ – supported by a $\sim$20 nm thick gold nanorod can be tuned from 650 nm to 1100 nm by changing its length from $L = 50$ nm to $L = 130$ nm [8]. This first dipolar mode is activated when the nanoantenna's length matches half of the effective wavelength of the charge oscillations inside the material's system, that is, $L = \lambda_{\mathrm{eff}}/2$. The LSPR effective wavelength's λ_{eff} depends on the nanoantenn'as shape and composition, and is related to the associated wavelength of the free-space radiation that couples with the first dipolar mode, $\lambda^{(1)}_{\mathrm{LSPR}}$, as [42]

$$\lambda_{\mathrm{eff}} = n_1 + n_2 \cdot \frac{\lambda^{(1)}_{\mathrm{LSPR}}}{\lambda_{\mathrm{p}}} \tag{3}$$

where λ_{p} is the metal plasma's wavelength ($\lambda_{\mathrm{p}} = 138$ nm for gold), n_1 and n_2 are coefficients with dimension of length that depends on the nanostructure's geometry and dielectric properties [42]. For the specific empirical case of gold nanorods cited above, $n_1 = -197$ nm and $n_2 = 63$ nm. Thus, the relation between the wavelength of the incident radiation that activates LSPR$^{(1)}$ and the nanoanetenna's size is given by $\lambda^{(1)}_{\mathrm{LSPR}}\,(\mathrm{nm}) = 431\ \mathrm{nm} + 4.37 \cdot L\,(\mathrm{nm})$, assuming a gold nanoantenna's thickness of 20 nm.

Equation (3) is a generic relation that can be analytically shaped for distinct morphologies, such as ellipsoids [42] and cones [43], by solving the Laplace's equation [6], [41] within the electrostatic approximation. Besides, similar procedures can be extended to more complex structures by computer simulations, providing information about the LSPR modes' energies as a function of its complex dielectric function, size and shape, as well as the dielectric function of the surrounding medium. This subject is covered in more details in Section IV-D.

At early stages, the application of LSPR-based nanoantennas on TERS was attempted with the construction of dielectric probes with metallic nanospheres attached to their apex. The diameter of the nanospheres was designed to match the right condition for LSPR$^{(1)}$, leading to spectral signal enhancement of $M_{\mathrm{TERS}} \sim 80$ [44], [45]. Latter on, more complex nanostructures were designed and applied on TERS experiments, such as gold nanocones leading to $M_{\mathrm{TERS}} \sim 1{,}200$ [46] and aluminum nanorods leading to $M_{\mathrm{TERS}} \sim 3{,}000$ [47]. Generally speaking, the LSPR effect achieves greater spectral signal enhancements than the LRE alone. It is important noticing that high values of field enhancement can increase the local temperature for hundreds of Celcius degrees, affecting the tip's morphology which, in turn, can shift the plasmon resonance away from the excitation laser energy [48], [49]. Therefore, if the laser power density is not carefully adjusted, the spectral signal enhancement

can be weakened during a TERS experiment due to local tip or sample heating.

Although $\lambda_{\rm eff} < \lambda_{\rm LSPR}$ at near-infrared and visible spectrum range, the LSPR modes can be directly excited by light, regardless the wavevector mismatch [6], [41]. This is an important advantage over the SPP schema.

D. Gap Plasmon

Another type of resonant optical nanoantenna can be obtained in the gap-mode configuration, in which the sample is "sandwiched" between a metallic tip and a metallic substrate, as illustrated in Fig. 1(d). When the tip is irradiated with an electric field polarized parallel to its shaft, an oscillating electric dipole is created at its apex and, in turn, an image dipole with opposite charge is produced at the metallic substrate (Fig. 1(d)) [18].

The proximity of the tip to the metallic substrate is the key parameter to control the matching between the gap plasmon mode and the excitation radiation field, as well as to improve the lateral resolution of the TERS image beyond the size of the tip's apex [20], [21], [50]. For a given wavelength of incident light, $\lambda_{\rm eff}$ decreases with the tip-sample separation distance (t) [51]. Weak enhancements can be observed at $t \simeq 10$ nm, and relatively high values are achieved at $t \simeq 1$ nm [18], [20]. The signal enhancement factor ($M_{\rm TERS} \simeq f_{\rm e}^4$) is expected to be improved up to 16 times (Au tip and Ag substrate) with $\lambda_{\rm laser} = 633$ nm, and up to 64 times (Ag tip and Ag substrate) with $\lambda_{\rm laser} = 532$ nm, both at a tip-sample distance $t = 1$ nm, where the gap plasmon effect becomes predominant [52]. The lateral confinement (w) of the enhanced field's hot spot scales with t in the form $w \propto \sqrt{R\,t}$, where R is the radius of the apex [20], [53]. Due to the onset of the quantum tunneling, ultimate lateral confinement is expect to happen at $t \sim 0.3$ nm, corresponding to $w \propto 2.7$ nm for $R = 10$ nm [20]. However, TERS images with higher levels of spatial resolution have been reported in the literature [21], [54]–[57]. In this quantum regime, whereas the cavity-field-driven signal would be expected to drop by about two orders of magnitude, the Raman scattering intensity grows by about two orders of magnitude [57]. In addition, atomic-scale subnanometer structures can be produced at the tip apex, leading to picocavities stabilized at cryogenic temperatures. This configuration is known to generate optical confinement at the angstrom scale [58].

Because the substrate must be metallic and the sample has to be placed in the closest distance as possible from the tip, gap plasmon resonances are usually achieved in TERS experiments performed in scanning tunneling microscopy (STM) mode. TERS images with ~ 1.7 nm of lateral resolution of carbon nanotubes sitting on a gold substrate have been obtained in an ambient STM-TERS conjugated system using gold tips as nanoantennas working in gap plasmon mode [55]. To push further the spatial resolution, low-temperature ultrahigh-vacuum (UHV) STM-based TERS systems can be used. Liao *et al.* reported the use of silver tips and substrates to perform TERS imaging of carbon nanotubes with sub-nanometric resolution ($\simeq 0.7$ nm) under base pressure of $\sim 1 \times 10^{-10}$ Torr at ~ 79 K [56]. Using the same equipment and conditions, Zhang *et al.* reported the TERS analysis of single molecules with lateral resolution of 0.5 nm, which was considered as the record of optical spatial resolution at that time [54]. To achieve this condition, the authors adjusted the tip-sample separation t to spectrally tune the gap plasmon mode with the Raman Stokes peak frequencies. Most recently, Lee *et al.* used similar setup and configurations, with Ag tip-Cu sample, to visualize vibrational normal modes of single molecules [57]. The spatial resolution achieved in this case was 0.17 nm, with tunnelling gap of $t = 0.2$ nm, which may be the current record.

It is important noticing that low-temperature UHV-STM-based TERS systems are complex equipment that require special sample preparation, thus not being a lab-routine tool for daily nanomaterial's characterization yet. Ordinary, STM-based or AFM-based TERS systems designed for ambient conditions are considerably simpler to operate. However, in the case of AFM, special attention must be paid if the metallic substrate presents topography flaw in the nanoscale. For instance, by decreasing the tip-sample distance in a conventional AFM-based setup, the field enhancement mediated by gap plasmon may overcome the signal enhancement by other mechanisms, such as LSPR or LRE. If in one hand this means better signal enhancement and possible improvement in spatial resolution, on the other, it can generate artifacts. In the case of a rough metallic substrate, the gap-plasmon between the tip and the substrate can lead to artificially-generated ultra-high spatial resolution, as observed by H. Miranda *et al.* [50]. By performing TERS experiments on monolayer graphene sandwiched between the apex of a gold tip and a substrate composed of a set of spherical gold nanoparticles, the authors observed artificial super-resolution, beyond the size of the tip apex' diameter [50].

IV. TERS Optical Nanoantennas Engineering

The first aspect to be considered during the design and fabrication of optical nanoantennas for TERS is the material composition. Morphology should also be taken into account to provide of the right conditions for the occurrence of plasmon resonance modes in nanoantennas, necessary for obtaining enough signal enhancement in TERS experiments. Another important aspect to be observed is the type of scanning probe microscopy (SPM) feedback mechanism used in the TERS setup. These subjects will be discussed in the following sections.

A. Material Composition

As described in Section III, except for the non-resonant LRE, the other field-enhancement mechanisms commonly employed in TERS (SPP, LSPR, and gap plasmon) require the metallic nanostructure to support surface plasmon (SP) resonances in the visible range. However, for nano-particles, SP resonance is only allowed within the range for which the real part of the dielectric constant is < -2 [12]. This upper limit lies in the infrared range for most metals. The few exceptions include gold ($\lambda \sim 500$ nm), silver ($\lambda \sim 365$ nm), copper ($\lambda \sim 350$ nm), platinum and aluminum (both occurring in the UV range) [60]–[62]. Additionally, if the incident radiation carries sufficient energy, interband electron transitions can occur, increasing plasmon

damping. Thus the wavelength of onset for interband transition ($\lambda_{\rm int}$) becomes an extra virtual limit, given the rapid increase of the imaginary part of the dielectric function. This is specially important for gold ($\lambda_{\rm int} \sim$530 nm) and copper ($\lambda_{\rm int} \sim$590 nm) [63].

For the reasons explained above, both real and imaginary parts of the dielectric function, $\varepsilon'(\lambda)$ and $\varepsilon''(\lambda)$, respectively, are important figures of merit for the indication of quality in plasmonic properties. While $\varepsilon''(\lambda)$ is related to the surface plasmon damping, $\varepsilon'(\lambda)$ indicates if SP resonances are allowed to happen. Empirically, the quality factor can be defined as the ratio between the enhanced electric local field and the incident electric field. However, a more specific definition that includes $\varepsilon'(\lambda)$ and $\varepsilon''(\lambda)$ must also take into account morphological aspects. For example, the quality factor for LSPR ($Q_{\rm LSPR}$) in an ellipsoid is given by $Q_{\rm LSPR} = \varepsilon'(\lambda)^2/\varepsilon''(\lambda)$ [63]. Although evaluated from a different definition, the same result holds for SPP [63], [64]. For $\lambda_{\rm laser} = 632.8$ nm, $Q_{\rm LSPR} \sim$110 for gold, $\sim$670 for silver, and $\sim$70 for copper [60]. For aluminum, $Q_{\rm LSPR} \sim$140, but the imminent formation of an alumina layer over the metallic surface strongly degrade its optical properties [62]. Platinum shows higher damping at this frequency range due to interband electron transitions, thus presenting much lower quality factor [65]. Judging from the quality factor, silver would be the best material to compose a resonant optical nanoantenna for TERS, if it was not for its high chemical instability in ambient conditions. For presenting the best compromise between quality factor and chemical stability, gold is still the most used metal for plasmonics, although its application is limited to longer wavelengths considering the spectrum of visible light (from yellow to red).

B. Fabrication Methods

1) Contact- Or Tapping-Mode AFM-Based TERS: A contact- or tapping-mode AFM-based TERS system requires cantilever-based probes. For that purpose, commercially available standard silicon oxide or silicon nitride cantilever tips can be covered with a thin layer of gold or silver by pulsed electrodeposition [66] or physical vapor deposition [16], [18]. The counterintuitive idea is not to create a smooth metallic coating, but a non-uniform film composed by nanoparticles. This schema is based on the expectation that an isolated nanoparticle located at the apex of the tip will have the right size and shape to support LSPR that matches the wavelength of the incident laser used in the TERS experiment [16]. For example, Taguchi *et al.* compared signal enhancement factors using SiO_2 AFM tips coated with smooth and rough Ag layers. The signal enhancement factor was derived from the TERS signal obtained from a graphene sample. The wavelength of the incident laser used in this experiment was $\lambda_{\rm laser} = 488$ nm. The authors found $M_{\rm TERS} \sim$65 and 3,500 for the smooth and rough Ag-coatings, respectively. In the smooth-coating case, the enhancement mechanism was solely addressed to the LRE. In the rough-coating case, the enhancement was addressed to LSPR combined to gap plasmon [67]. This method has been proved feasible, providing TERS images with sub-30 nm spatial resolution [68], [69]. The main drawback is the low-rate of reproducibility of the optical performance, since the metallic nanoparticles formed in rough Ag films present broad distributions of size and shape.

2) STM-Based TERS: As explained in section III-D, field enhancement in STM-based TERS systems is usually mediated by gap plasmon modes. For that, any type of clean gold or silver tips with small apex sizes are suficient [21], [68].

3) Shear Force AFM-Based TERS: In the shear force AFM-based TERS, the probe is attached to a quartz tuning fork. The feedback mechanism is based on the tuning fork's resonance frequency. This schema was created at the early stage of SNOM's developement, and was firstly employed to use an elongated optical fiber as a SNOM probe, without distorting the topographic image [70]. It opened the possibility of creating a broad range of tip designs, keeping good tip-sample separation control.

The most common fabrication process reported in the literature for nanoantennas used in shear-force AFM-based TERS is the electrochemical etching of gold wires [71]. For that, a wire of $\simeq 50$ μm of diameter, acting as an electrode, is dipped into an etching solution, usually fuming HCl, at the center of a platinum counter electrode ring. An applied AC+DC voltage between the electrodes induces an etching process at the meniscus, until the bottom part of the wire is droped, leaving a nanometer sized to a sharp gold tip at the remaining part [72]. This process is hardly reproducible due to random variations in the etching parameters [16]. Nevertheless, smooth solid gold tips with apex diameters of $\lesssim$30 nm can be fabricated with this method, as shown in the scanning electron microscopy (SEM) images depicted in Fig. 2(a)–(e).

As mentioned before, a smooth gold tip – as the one illustrated in Fig. 2 – provides signal enhancement through the LRE, for which relatively weak field enhancement is expected. However, relatively high signal enhancement factors have been reported in the literature for TERS experiments using this type of gold tip – e.g. $M_{\rm TERS} \sim$1,015 [73] and $M_{\rm TERS} \sim$1,145 [13], for TERS experiments performed on carbon nanotubes. The most probable explanation for the low-yield achievement of such high signal enhancement factors lies on a fortuitous formation of surface flaws close to the tip apex, which may act as plasmon's confinement sites, leading to LSPR mode-matching with the wavelength of the excitation radiation field. Counterintuitively, the greater the roughness or flaws on the tip's surface, the greater the chance of matching the LSPR condition, thereby resulting in better TERS image quality.

Indeed, instabilities during the etching process can generate deformations on the tip's surface, as shown in Fig. 2(b). Besides that, grain boundaries can create surface discontinuation due to the anisotropy of the etching rate, which strongly depends on the crystal's orientation. Fig. 2(c) shows an electron backscatter diffraction (EBSD) image superposed to an SEM image of an etched gold tip. The image reveals the presence of grain boundaries defining sites with distinct orientations. This phenomenon can be used to improve the optical efficiency of etched gold tips. By annealing the gold wire prior to the electrochemical etching process, its polycrystalline structure can be turned into a mosaic

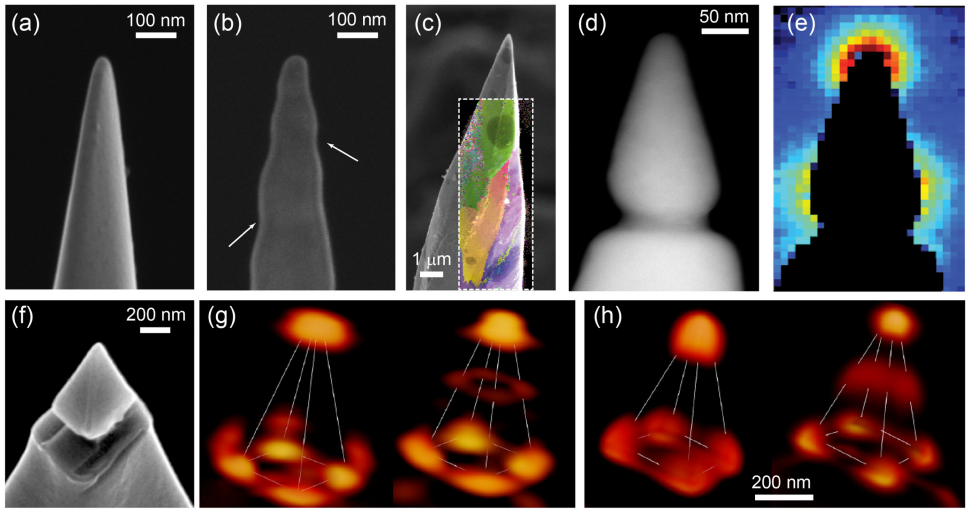

Fig. 2. Morphology, microstructure and plasmonic features of pristine and nano-patterned electrochemical etched gold tips. (a) and (b) are SEM images showing a regular smooth sharp tip and a slightly deformed tip, respectively. (c) EBSD microstructural image overlaying the corresponding SEM image of an etched gold tip. The color scale renders distinct crystal orientations. (d) TEM image of a FIB-modified tip. (e) 2D-EELS map of the same tip as in (d), recorded within the 2.1 eV energy window, corresponding to the LSPR 1^{st} mode. Reproduced with permission from ref. [3]. (f) SEM image of a HIM-modified etched gold tip and its (g) 3D-reconstructed EELS map at the LSPR 1st and 2nd modes (left and right, respectively). (h) Corresponding EELS simulation via MNPBEM code. Reproduced with permission from ref. [59].

of well defined nano-crystal domains [74] able to support LSRP modes.

Energy-loss spectroscopy (EELS) performed in a transmission electron microscope (TEM) is a powerful technique to investigate the tip's ability to support LSPR modes. EELS spectra acquired at the vicinity of the tip apex can reveal the presence of LSPR-related absorption peaks. Moreover, EELS maps spectrally-tuned to those peaks indicate the energy of the LSPR dipolar mode [3].

C. FIB and HIM Applied to Nanoantenna Design

A possible route to control LSPR modes in optical nanoantennas is the application of a focused Ga-ion beam (FIB) to directly design plasmonic features on the metallic surface. We have demonstrated that a single transversal groove, milled by FIB in a position near the apex of an etched gold tip, acts as an obstacle that defines a plasmonic cavity capable of supporting LSPR in the visible and near-infrared ranges [3]. This structure is illustrated in Fig. 2(d). EELS performed on a TEM was used to obtain highly spatially- and spectroscopically-resolved electron-loss energy maps that reveal LSPR dipolar modes of the milled gold tip (Fig. 2(e)). Similar measurements were performed on different milled probes, whose grooves were drawn in different distances, L, measured from the tip's apex [3]. The results were used to define a linear relation between the energy of the 1^{st} LSPR dipolar mode – LSPR$^{(1)}$ – and the characteristic length L. By changing the distance L between the groove and the apex of the probe, the LSPR$^{(1)}$ can now be fine-tuned to match a desired absorption channel.

The grooved nanoantenna was tested in a TERS experiment performed on a graphene sample. The TERS signal was first measured with a smooth etched gold tip. The same tip was FIB-milled, and a groove was drawn 240 nm far from its apex, which was the optimal length defined by the EELS measurements to reach the match between LSPR$^{(1)}$ and the wavelength of the incident HeNe-laser used in the experiment ($\lambda_{laser} = 632.8$ nm). The optical efficiency improved $\sim$5.5 times in the presence of the milled groove, compared with the original smooth tip. The result demonstrates the advantage of incorporating LSPR to conventional TERS tapered gold tips.

Later on, Archanjo *et al.* showed the possibility of improving the quality of the milling process by using a helium-ion microscope (HIM), instead of a Ga-FIB (Fig. 2(f)) [59]. Using this high-precision tool, the original conical shape of the apex was redesign, turned into a pyramid tip with sharper apex, and a well-defined groove few hundred nanometers far from the apex. Furthermore, the LSPR features were analyzed through the 3D-reconstruction of a set of 2D-EELS maps, showing that the LSPR hot spots are located at the pyramid's lateral edges and corners (Fig. 2(g)).

D. Modelling and Simulation

Theoretical analysis can be used to understand the plasmonic properties of nanostructures, as well as to guide the development of new types of plasmonic nanoantennas with different materials and morphologies, specially designed to match the target applications. The major difficulty in this field is related to the fact that most of the calculations do not have analytical solution. In this scenario, computer simulations prove to be a good alternative for finding structural vs. resonant energies, or to simulate field enhancement tendencies. The main drawback is the relatively high computational cost. The simulation of plasmonic nanoantennas usually relies on solving Maxwell's equations for complex structures, where the object's morphology and dielectric function are the code inputs. The most used methods are: finite difference time domain (FDTD) [75],

[76], discontinuous Galerkin time-domain (DGTD) [77], [78], discrete dipole approximation (DDA) [3], [77] and boundary element method (BEM) [59], [79], [80].

In comparison with DDA and FDTD simulations, the BEM approach is less flexible, but still useful for optical nanoantennas in most of the cases, which involve homogeneous dielectric media and abrupt boundaries. BEM performs faster and demands less RAM memory than DDA and FDTD, because the former uses boundary discretization (number of elements grows with area), which is lighter in comparison with the volume discretization of DDA and FDTD (number of elements grows with volume). Additionally, the development of potential-based BEM [79] has a linear gain, since the size of the matrices have a number N of surface elements, smaller than the $3N$ elements present in field-based BEM schemes [80]. Reducing the number of discretization elements is important for keeping the feasibility of simulations involving plasmonic nanoantennas for TERS, given that they have typical sizes in the order of a few hundred nanometers, which is much larger than other conventional plasmonic nanostructures.

In previous studies, we have used both DDA [3] and BEM (MNPBEM-metal nanoparticle BEM approach) [5], [59], to understand the relation between the LSPR energy modes and the nanoantenna's morphological parameters, including material composition, shape (opening angle), and size. We have found that sharp tips (low opening angle) suppress LSPR modes in the visible range [59]. Additionally, 3D LSPR information was recorded from simulations of 2D EELS maps for pyramidal tips rotated at different angels, and the theoretical results (Fig. 2(h)) have excellent agreement with the experimental 3D EELS reconstruction (Fig. 2(g)) [59].

E. Plasmon-Tunable Tip Pyramid

The major drawback of producing nanoantennas through electrochemical etching is that the reproducibility rate is extremely low, being unsuitable for large-scale batch production. A viable alternative was recently presented with the production of template-stripped gold micropyramids, specially adapted to be used as nanoantennas in a shear-force AFM-based TERS setup [37]. The process starts with the formation of micropyramidal cavities on a silicon substrate via lithography. Then, the cavities are used as templates for shaping the gold micropyramid tip. The method is based on two pillars [81]. The first is the low adherence of gold to silicon, which permits the lift-out process of the evaporated gold micropyramid from the silicon cavity without causing structural damage. The second is the highly anisotropic chemical etching of silicon along different crystallographic planes, which permits the formation of the pyramidal-shaped cavities. The etching process is mediated by a KOH aqueous solution (30% wt.) at 70 °C, and takes place over circular-shaped etching masks defined by optical lithography over Si_3N_4 cover layer. The walls of the pyramidal cavities are made of [111] crystal planes, and the summit has an open semi-angle of $\phi \sim 35.2^{\circ}$.

The nanoantennas made of template-stripped gold micropyramids present moderate signal enhancement factor ($M_{\mathrm{TERS}} \sim$150 [37], $M_{\mathrm{TERS}} \sim$460 [5]) with high-reproducibility rate [37]. However, because the pyramidal gold walls are smooth and featureless, they are not able to hold any type of plasmon resonance. In this case, the only possible mechanism of field enhancement is the LRE. To improve this aspect, a new template-stripe method based on a two-step lithography process that generates a micropyramidal body with a nanopyramid end was introduced in Ref. [5]. The resulting structure is shown in Figs. 3(a)–(c). The length L of the nanopyramid tip (Fig. 3(c)) is dimensioned to fine-tune LSPR modes, giving rise to a plasmon-tunable tip pyramid (PTTP) [84]. The plasmonic properties of this probe were studied by EELS and MNPBEM simulations, reveling that PTTPs act as monopole nanoantennas [5]. In short, the nanopyramidal part is electrically grounded on a flat plateau that acts as a mirror that provides the monopole's image, as illustrated in Fig. 3(d).

Several PTTPs with distinct nanopyramid characteristic lengths, L, were tested in TERS experiments performed on a graphene monolayer excited with a HeNe laser source ($\lambda_{\mathrm{laser}} = 632.8$ nm). The results showed a $M_{\mathrm{TERS}} \sim$5,100 for $L \sim$470 nm, which matches the LSPR 2^{nd} monopole mode ($L = \frac{3}{4}\lambda_{\mathrm{eff}}$) [5]. This gain is at least 11-fold larger than the maximum gain reported for bare template-stripped gold micropyramids [5], showing that LSPR is a powerful mechanism to achieve high levels of signal enhancement with excellent reproducibility rate.

Fig. 4 presents the results of TERS experiments performed on mechanically exfoliated graphene samples, using PTTP nanoantennas tuned with the incident HeNe laser ($L \sim$470 nm for $\lambda_{\mathrm{laser}} = 632.8$ nm). In Fig. 4(a), the Raman spectra were acquired with and without the PTTP to evaluate the signal enhancement factor at the center of the monolayer graphene flake. The measured values of spectral signal enhancement were $F_{\mathrm{TERS}} = 72$ for the two-phonon totally symmetric 2D band (occurring at $\sim$2,700 cm^{-1}), and $F_{\mathrm{TERS}} = 24$ for the first-order bond-stretching G band (occurring at $\sim$1,580 cm^{-1}). The difference in the signal enhancements observed for these two bands is due to coherence effects related to the symmetries of the associated vibrational modes [23]. To the best of our knowledge, the 72-fold spectral signal enhancement achieved in this experiment is by far the greatest TERS enhancement achieved in a 2D material to date.

Fig. 4(b) shows the TERS results extracted from a $1.28\,\mu$m-long hyperspectral scan line taken across the edge of a monolayer graphene. The graphic depicts the intensities of the 2D and D peaks recorded along the scan line, as well as for another unknown peak observed at $1{,}146$ cm^{-1}. The signal of the 2D peak (dark blue) is roughly constant inside the flake, abruptly dropping when moving across the edge (■ position). The drop was used to estimate a lateral spatial resolution of $\sim$10 nm (10% to 90% of signal variation). The D band occurs at $\sim$1350 cm^{-1}, and is activated by the presence of structural defects. Its TERS intensity profile (green line) presents two features near the edge, each of them with $\sim$10 nm of full width at half maximum (FWHM). An extra par of peaks (spectrally centered at

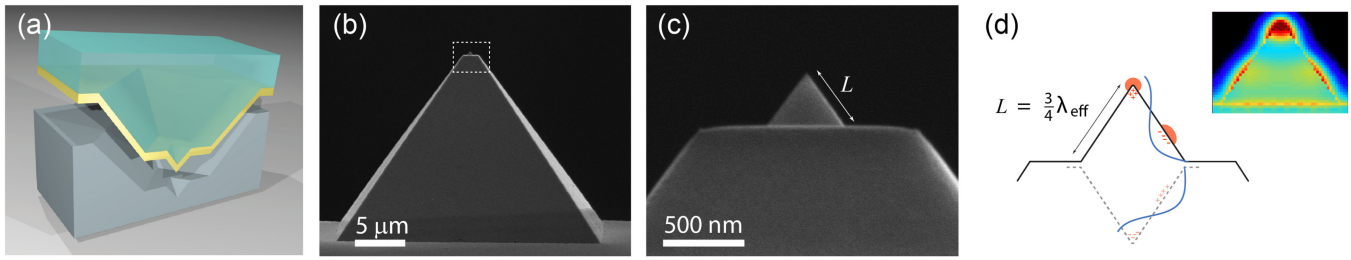

Fig. 3. Illustration of plasmon-tunable tip pyramid (PTTP) monopole nanoantennas' fabrication and characterization. (a) Illustration of a cross-section view of the template-stripe method used to fabricate the PTTP's (color scale: silicon - gray, gold - yellow and epoxy glue - cyan). Reproduced with permission from ref. [5]. (b) SEM image showing the whole pyramid body of a PTTP nanoantenna fixed on a tungsten wire after been template-striped from the silicon substrate. (c) Zoomed SEM image showing details of the nanopyramid on the top of the PTTP's plateau. The edge's dimension L is indicated. (d) Schematics (left) and simulated EELS map (right) showing the monopole character of the LSPR in the PTTP. The schematics illustrates the relation between L and the plasmon effective's wavelength. The inset is the result of a MNPBEM simulation map, considering the 2nd LSPR monopole mode. Hot colors indicate strong field enhancement.

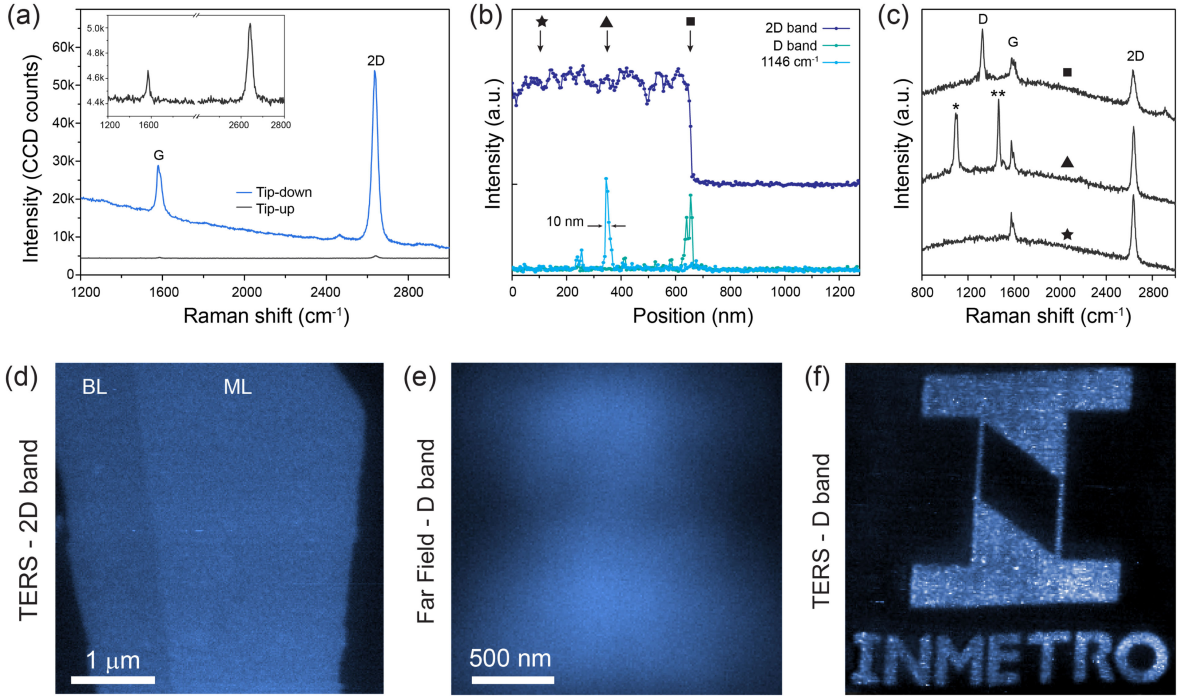

Fig. 4. TERS experiemnts performed on a exfoliated graphene sample using PTTP optical nanoantennas. (a) Representative tip-up (black) and tip-down (blue) Raman spectra using a PTTP nanoantenna. The inset shows details on the tip-up Raman spectrum. (b) Hyperspectral line profile recorded across the edge of the graphene flake. The lines render the intensities of the 2D band (dark blue), the D band (green), and the unknown 1,146 cm^{-1} band originated from a contamination spot (ligth blue). (c) Raman spectra recorded at the positions indicated by the respective symbols in panel (b). (d) TERS image rendering the 2D band intensity of a graphene flake formed by two different regions: a bilayer (BL) and a monolayer (ML). (e) Conventional confocal far-field Raman image and (f) TERS image rendering the D Raman band intensity of a graphene sample nano-patterned by HIM. The bright area is a defective spot shaped with the Inmetro's logotype. The image in (f) was obtained using a PTTP resonant nanoantenna with $L = 460$ nm. Details about the experimental apparatus can be found in [82], [83].

1,146 cm^{-1} and 1,466 cm^{-1}), probably related to a local contamination spot, were observed at a specific position (▲) inside the graphene area, located approximately 300 nm far from the edge. The intensity line profile related to the 1,146 cm^{-1} feature (light blue) presents a sharp spike with FWHM of $\sim$10 nm, corroborating with the lateral resolution measured from the 2D band line profile. Fig. 4(c) presents the TERS spectra acquired in three specific regions: the edge of the graphene flake (■), the contamination spot on the grapehen area (▲), and the pristine graphene (★).

Next, we evaluate the signal enhancement factor for the PTTP used in the experiment shown in Fig. 4. The radius of the area below the tip can be estimated from the lateral resolution achieved in the experiment, which is $R_{\mathrm{NF}} = 10$ nm. The radius of the area measured without the tip is defined by the incident laser focus area, being $R_{\mathrm{NF}} \simeq 275$ nm for this specific optical system [5]. Finally, a signal enhancement of $F_{\mathrm{TERS}} = 72$ was obtained for the TERS signal of the 2D band. By inserting these values in Eq. (2), we obtain a signal enhancement factor $M_{\mathrm{TERS}} = 53{,}690$. This value is two orders of magnitude higher than the values typically achieved with non-resonant nanoantennas. Such a high optical efficiency provides the possibility of performing TERS images of two dimensional systems with outstanding near-field to far-field contrast. Fig. 4(d) shows a TERS image of a graphene sample, where the color scale renders the 2D band intensity. The image was obtained using a PTTP

with $L = 490$ nm, and a HeNe laser as the incident light source. Besides the sharp graphene edges, one can clearly distinguish the monolayer (ML) region from the bi-layer (DL) region.

Finally, the capability of the PTTPs to perform optical imaging with high spatial resolution was tested in a mechanically exfoliated few-layer graphene that underwent a nano-patterning process by HIM. We have used a focused He ion beam to drawn a defective area that reproduces the logo of the Brazilian Institute of Metrology (Inmetro). The pattern was produced with a low dose (1×10^{16} ions/nm^2) to create fine defects lines, avoiding intense erosion regions. Fig. 4(e) and (f) show Raman spectral images of the intensity of the D band without (confocal Raman) and with (TERS), respectively, the presence of a PTTP resonant nanoantenna with $L = 460$ nm.

V. Conclusion

A summary of applications of optical nanoantennas as efficient probes for TERS was presented. The probes are responsible for both emission and collection of incident and scattered radiation. Because TERS involves extremely week scattered fields originated from tiny areas, the optical efficiency of the nanoantenna is a crucial quality factor in the TERS technology. To achieve a satisfactory degree of quality, the nanoantenna should support plasmon resonances tuned to the incident laser used in the TERS measurement. The main resonant mechanisms are the surface plasmon polaritons (SPP), the local surface plasmon resonance (LSPR), and the plasmon gap mode. To activate one of these mechanisms, nanoantenna engineering is necessary to adequate the nanoantenna's size, shape and composition to the wavelength of the incident laser light used in the TERS experiment. Computational simulation is an important tool to guide the development of new types of plasmonic nanoantennas with different materials and morphologies, specially designed to match the target applications. A complete overview on the recently developed nanoantenna composed of a micropyramidal body with a nanopyramid end was presented. The length L of the truncated nanopyramid tip is dimensioned to fine-tune LSPR modes, giving rise to a plasmon-tunable tip pyramid (PTTP). The plasmonic properties of this probe were studied by EELS and MNPBEM simulations, reveling that PTTPs act as monopole nanoantennas. TERS results obtained with PTTPs demonstrated the achievement of unprecedented levels of field enhancement - mediated by LSPR - with excellent reproducibility rate. While the high optical efficiency allows for new applications with versatility (faster imaging), the reproducibility raises the reliability of TERS to the level of becoming a metrological tool for nanomaterials science and technology.

References

[1] P. Muehlschlegel, H.-J. Eisler, O. J. Martin, B. Hecht, and D. Pohl, "Resonant optical antennas," *Science*, vol. 308, no. 5728, pp. 1607–1609, 2005.

[2] L. Novotny and N. Van Hulst, "Antennas for light," *Nature Photon.*, vol. 5, no. 2, pp. 83–90, 2011.

[3] T. L. Vasconcelos *et al.*, "Tuning localized surface plasmon resonance in scanning near-field optical microscopy probes," *ACS Nano*, vol. 9, no. 6, pp. 6297–6304, 2015.

[4] T. H. Taminiau, R. J. Moerland, F. B. Segerink, L. Kuipers, and N. F. van Hulst, "λ/4 resonance of an optical monopole antenna probed by single molecule fluorescence," *Nano Lett.*, vol. 7, no. 1, pp. 28–33, 2007.

[5] T. L. Vasconcelos *et al.*, "Plasmon-tunable tip pyramids: Monopole nanoantennas for near-field scanning optical microscopy," *Adv. Opt. Mater.*, vol. 6, no. 20, 2018, Art. no. 1800528.

[6] K. L. Kelly, E. Coronado, L. L. Zhao, and G. C. Schatz, "The optical properties of metal nanoparticles: The influence of size, shape, and dielectric environment," *J. Phys. Chem. B*, vol. 107, no. 3, pp. 668–677, 2003.

[7] P. K. Jain, X. Huang, I. H. El-Sayed, and M. A. El-Sayed, "Noble metals on the nanoscale: Optical and photothermal properties and some applications in imaging, sensing, biology, and medicine," *Accounts Chem. Res.*, vol. 41, no. 12, pp. 1578–1586, 2008.

[8] S. Wang *et al.*, "Three-photon luminescence of gold nanorods and its applications for high contrast tissue and deep in vivo brain imaging," *Theranostics*, vol. 5, no. 3, pp. 251–266, 2015.

[9] B. Zeng, Y. Gao, and F. J. Bartoli, "Ultrathin nanostructured metals for highly transmissive plasmonic subtractive color filters," *Scientific Rep.*, vol. 3, pp. 2890–2849, 2013.

[10] E. Petryayeva and U. J. Krull, "Localized surface plasmon resonance: Nanostructures, bioassays and biosensing-A review," *Analytica Chimica Acta*, vol. 706, no. 1, pp. 8–24, 2011.

[11] X. Huang, I. H. El-Sayed, W. Qian, and M. A. El-Sayed, "Cancer cell imaging and photothermal therapy in the near-infrared region by using gold nanorods," *J. Amer. Chem. Soc.*, vol. 128, no. 6, pp. 2115–2120, 2006.

[12] L. Novotny and B. Hecht, *Principles of Nano-Optics*. New York, NY, USA: Cambridge Univ. Press, 2012.

[13] L. G. Cançado, A. Hartschuh, and L. Novotny, "Tip-enhanced Raman spectroscopy of carbon nanotubes," *J. Raman Spectrosc.*, vol. 40, no. 10, pp. 1420–1426, 2009.

[14] J. Stadler, T. Schmid, and R. Zenobi, "Nanoscale developments in and practical guidelines for tip-enhanced Raman spectroscopy," *Nanoscale*, vol. 4, pp. 1856–1870, 2012.

[15] N. Mauser and A. Hartschuh, "Tip-enhanced near-field optical microscopy," *Chem. Soc. Rev.*, vol. 43, no. 4, pp. 1248–1262, 2014.

[16] T. Deckert-Gaudig, A. Taguchi, S. Kawata, and V. Deckert, "Tip-enhanced Raman spectroscopy—From early developments to recent advances," *Chem. Soc. Rev.*, vol. 46, no. 13, pp. 4077–4110, 2017.

[17] F. Shao and R. Zenobi, "Tip-enhanced raman spectroscopy: principles, practice, and applications to nanospectroscopic imaging of 2D materials," *Analytical Bioanalytical Chemistry*, vol. 411, no. 1, pp. 37–61, 2019.

[18] X. Shi, N. Coca-López, J. Janik, and A. Hartschuh, "Advances in tip-enhanced near-field raman microscopy using nanoantennas," *Chem. Rev.*, vol. 117, no. 4, pp. 4945–4960, 2017.

[19] I. O. MacIel *et al.*, "Electron and phonon renormalization near charged defects in carbon nanotubes," *Nature Mater.*, vol. 7, no. 11, pp. 878–883, 2008.

[20] S. F. Becker *et al.*, "Gap-plasmon-enhanced nanofocusing near-field microscopy," *ACS Photon.*, vol. 3, no. 2, pp. 223–232, 2016.

[21] S. Jiang *et al.*, "Subnanometer-resolved chemical imaging via multivariate analysis of tip-enhanced raman maps," *Light: Sci. Appl.*, vol. 6, no. 11, pp. e17098–e17098, 2017.

[22] R. Ossikovski, Q. Nguyen, and G. Picardi, "Simple model for the polarization effects in tip-enhanced raman spectroscopy," *Phys. Rev. B*, vol. 75, no. 4, 2007, Art. no. 045412.

[23] L. G. Cançado, R. Beams, A. Jorio, and L. Novotny, "Theory of spatial coherence in near-field Raman scattering," *Phys. Rev. X*, vol. 4, no. 3, 2014, Art. no. 031054.

[24] R. Beams, L. G. Cançado, S.-H. Oh, A. Jorio, and L. Novotny, "Spatial coherence in near-field raman scattering," *Phys. Rev. Lett.*, vol. 113, no. 18, 2014, Art. no. 186101.

[25] A. R. Neto *et al.*, "Protocol and reference material for measuring the nanoantenna enhancement factor in tip-enhanced Raman spectroscopy," in *Proc. 4th Int. Symp. Instrum. Syst., Circuits Transducers*, 2019, pp. 1–6.

[26] B. Pettinger, K. F. Domke, D. Zhang, G. Picardi, and R. Schuster, "Tip-enhanced Raman scattering: Influence of the tip-surface geometry on optical resonance and enhancement," *Surf. Sci.*, vol. 603, no. 10–12, pp. 1335–1341, 2009.

[27] R. S. Alencar *et al.*, "Probing spatial phonon correlation length in post-transition metal monochalcogenide GaS using tip-enhanced Raman spectroscopy," *Nano Lett.*, vol. 19, no. 10, pp. 7357–7364, 2019.

[28] D. W. Pohl, W. Denk, and M. Lanz, "Optical stethoscopy: Image recording with resolution λ/20," *Appl. Phys. Lett.*, vol. 44, no. 7, pp. 651–653, 1984.

[29] B. Hecht *et al.*, "Scanning near-field optical microscopy with aperture probes: Fundamentals and applications," *J. Chem. Phys.*, vol. 112, no. 18, pp. 7761–7774, 2000.

[30] R. Zenobi, R. M. Stockle, Y. D. Suh, and V. Deckert, "Nanoscale chemical analysis by tip-enhanced Raman spectroscopy," *Chem. Phys. Lett.*, vol. 318, no. 1–3, pp. 131–136, 2000.

[31] N. Hayazawa, Y. Inouye, Z. Sekkat, and S. Kawata, "Metallized tip amplification of near-field Raman scattering," *Opt. Commun.*, vol. 183, no. 1, pp. 333–336, 2000.

[32] S. Thomas, G. Wachter, C. Lemell, J. Burgdörfer, and P. Hommelhoff, "Large optical field enhancement for nanotips with large opening angles," *New J. Phys.*, vol. 17, no. 6, 2015, Art. no. 63010.

[33] L. Novotny, R. X. Bian, and X. S. Xie, "Theory of nanometric optical tweezers," *Phys. Rev. Lett.*, vol. 79, no. 4, pp. 645–648, 1997.

[34] M. Chaigneau, G. Picardi, and R. Ossikovski, "Molecular arrangement in self-assembled azobenzene-containing thiol monolayers at the individual domain level studied through polarized near-field Raman spectroscopy," *Int. J. Mol. Sci.*, vol. 12, no. 2, pp. 1245–1258, 2011.

[35] O. J. Martin and C. Girard, "Controlling and tuning strong optical field gradients at a local probe microscope tip apex," *Appl. Phys. Lett.*, vol. 70, no. 6, pp. 705–707, 1997.

[36] S. Thomas and M. Schenk, "Probing of optical near-ïňĄelds by electron rescattering on the 1 nm scale, Thomas 2012.pdf," *Nano Lett.*, vol. 13, no. 10, pp. 4790–4794, 2013.

[37] T. W. Johnson *et al.*, "Highly reproducible near-field optical imaging with sub-20-nm resolution based on template-stripped gold pyramids," *ACS Nano*, vol. 6, no. 10, pp. 9168–9174, 2012.

[38] A. V. Zayats, I. I. Smolyaninov, and A. A. Maradudin, "Nano-optics of surface plasmon polaritons," *Phys. Rep.*, vol. 408, no. 3, pp. 131–314, 2005.

[39] C. Ropers *et al.*, "Grating-coupling of surface plasmons onto metallic tips: A nanoconfined light source," *Nano Lett.*, vol. 7, no. 9, pp. 2784–2788, 2007.

[40] S. Berweger, J. M. Atkin, R. L. Olmon, and M. B. Raschke, "Light on the tip of a needle: Plasmonic nanofocusing for spectroscopy on the nanoscale," *J. Phys. Chem. Lett.*, vol. 3, no. 7, pp. 945–952, 2012.

[41] S. A. Maier, *Plasmonics: Fundamentals and Applications*. Berlin, Germany: Springer, 2007.

[42] L. Novotny, "Effective wavelength scaling for optical antennas," *Phys. Rev. Lett.*, vol. 266802, pp. 1–4 2007.

[43] N. Talebi *et al.*, "Excitation of mesoscopic plasmonic tapers by relativistic electrons: Phase matching versus eigenmode resonances," *ACS Nano*, vol. 9, no. 7, pp. 7641–7648, 2015.

[44] P. Bharadwaj and L. Novotny, "Spectral dependence of single molecule fluorescence enhancement," *Opt. Express*, vol. 15, no. 21, pp. 14266–14274, 2007.

[45] P. Bharadwaj and L. Novotny, "Plasmon-enhanced photoemission from a single Y3N@C80 fullerene," *J. Phys. Chem. C*, vol. 114, no. 16, pp. 7444–7447, 2010.

[46] M. Fleischer *et al.*, "Gold nanocone near-field scanning optical microscopy probes," *ACS Nano*, vol. 5, no. 4, pp. 2570–2579, 2011.

[47] L. Neumann, J. van't Oever, and N. F. van Hulst, "A resonant scanning dipole-antenna probe for enhanced nanoscale imaging," *Nano Lett.*, vol. 13, no. 11, pp. 5070–5074, 2013.

[48] A. Ambrosio *et al.*, "Shape dependent thermal effects in apertured fiber probes for scanning near-field optical microscopy," *J. Appl. Phys.*, vol. 99, no. 8, 2006, Art. no. 084303.

[49] M. Richard-Lacroix and V. Deckert, "Direct molecular-level near-field plasmon and temperature assessment in a single plasmonic hotspot," *Light: Sci. Appl.*, vol. 9, no. 1, pp. 1–13, 2020.

[50] H. Miranda *et al.*, "Impact of substrate on tip-enhanced Raman spectroscopy: A comparison between field-distribution simulations and graphene measurements," *Phys. Rev. Res*, vol. 2, no. 2, Jun. 2020, Art. no. 023408.

[51] H. T. Miyazaki and Y. Kurokawa, "Squeezing visible light waves into a 3-nm-thick and 55-nm-long plasmon cavity," *Phys. Rev. Lett.*, vol. 96, no. 9, pp. 1–4, 2006.

[52] N. Kazemi-Zanjani, S. Vedraine, and F. Lagugné-Labarthet, "Localized enhancement of electric field in tip-enhanced Raman spectroscopy using radially and linearly polarized light," *Opt. Express*, vol. 21, no. 21, 2013, Art. no. 25271.

[53] K. J. Savage *et al.*, "Revealing the quantum regime in tunnelling plasmonics," *Nature*, vol. 491, no. 7425, pp. 574–577, 2012.

[54] R. Zhang *et al.*, "Chemical mapping of a single molecule by plasmon-enhanced Raman scattering," *Nature*, vol. 498, no. 7452, pp. 82–86, 2013.

[55] C. Chen, N. Hayazawa, and S. Kawata, "A 1.7 nm resolution chemical analysis of carbon nanotubes by tip-enhanced Raman imaging in the ambient," *Nature Commun.*, vol. 5, pp. 1–5, 2014.

[56] M. Liao *et al.*, "Tip-enhanced Raman spectroscopic imaging of individual carbon nanotubes with subnanometer resolution," *Nano Lett.*, vol. 16, no. 7, pp. 4040–4046, 2016.

[57] J. Lee, K. T. Crampton, N. Tallarida, and V. A. Apkarian, "Visualizing vibrational normal modes of a single molecule with atomically confined light," *Nature*, vol. 568, pp. 78–82, 2019.

[58] F. Benz *et al.*, "Single-molecule optomechanics in 'Picocavities'," *Science*, vol. 354, no. 6313, pp. 726–729, 2016.

[59] B. S. Archanjo *et al.*, "Plasmon 3D electron tomography and local electric-field enhancement of engineered plasmonic nanoantennas," *ACS Photon.*, vol. 5, pp. 2834–2842, 2018.

[60] P. B. Johnson and R.-W. Christy, "Optical constants of the noble metals," *Phys. Rev. B*, vol. 6, no. 12, pp. 4370–4379, 1972.

[61] H. Ehrenreich, H. R. Philipp, and B. Segall, "Optical properties of aluminum," *Phys. Rev.*, vol. 132, no. 5, pp. 1918–1928, 1963.

[62] A. B. Djuris, J. M. Elazar, and M. L. Majewski, "Optical properties of metallic films for vertical-cavity optoelectronic devices," vol. 37, no. 22, pp. 5271–5283, 1998.

[63] P. R. West *et al.*, "Searching for better plasmonic materials," *Laser Photon. Rev.*, vol. 4, no. 6, pp. 795–808, 2010.

[64] K. M. McPeak *et al.*, "Plasmonic films can easily be better: Rules and recipes," *ACS Photon.*, vol. 2, no. 3, pp. 326–333, 2015.

[65] I. Zorić, B. Kasemo, C. Langhammer, and M. Zaaach, "Nanodisk plasmons : Material damping mechanisms," *ACS Nano*, vol. 5, no. 4, pp. 2535–2546, 2011.

[66] L. K. Yang *et al.*, "Rational fabrication of a gold-coated AFM TERS tip by pulsed electrodeposition," *Nanoscale*, vol. 7, no. 43, pp. 18225–18231, 2015.

[67] A. Taguchi, J. Yu, P. Verma, and S. Kawata, "Optical antennas with multiple plasmonic nanoparticles for tip-enhanced Raman microscopy," *Nanoscale*, vol. 7, no. 41, pp. 17424–17433, 2015.

[68] Y. Fujita, P. Walke, S. De Feyter, and H. Uji-i, "Tip-enhanced Raman scattering microscopy: Recent advance in tip production," *Japanese J. Appl. Phys.*, vol. 55, no. 8S1, 2016, Art. no. 08NA02.

[69] N. Kumar, B. M. Weckhuysen, A. J. Wain, and A. J. Pollard, "Nanoscale chemical imaging using tip-enhanced Raman spectroscopy," *Nature Protocols*, vol. 14, pp. 1169–1193, 2019.

[70] W. H. J. Rensen, N. F. van Hulst, A. G. T. Ruiter, and P. E. West, "Atomic steps with tuning-fork-based noncontact atomic force microscopy," *Appl. Phys. Lett.*, vol. 75, no. 11, pp. 1640–1642, 1999.

[71] B. Ren, G. Picardi, and B. Pettinger, "Preparation of gold tips suitable for tip-enhanced Raman spectroscopy and light emission by electrochemical etching," *Rev. Scientific Instrum.*, vol. 75, no. 4, pp. 837–841, 2004.

[72] S. S. Kharintsev, A. I. Noskov, G. G. Hoffmann, and J. Loos, "Near-field optical taper antennas fabricated with a highly replicable AC electrochemical etching method," *Nanotechnology*, vol. 22, no. 2, 2010, Art. no. 025202.

[73] L. G. Cançado *et al.*, "Mechanism of near-field Raman enhancement in one-dimensional systems," *Phys. Rev. Lett.*, vol. 103, no. 18, 2009, Art. no. 186101.

[74] D. Roy, C. M. Williams, and K. Mingard, "Single-crystal gold tip for tip-enhanced Raman spectroscopy," *J. Vac. Sci. Technol. B: Microelectron. Nanometer Struct.*, vol. 28, no. 3, pp. 631–634, 2010.

[75] A. F. Oskooi *et al.*, "MEEP: A flexible free-software package for electromagnetic simulations by the FDTD method," *Comput. Phys. Commun.*, vol. 181, no. 3, pp. 687–702, 2010.

[76] X. Li *et al.*, "Investigation on tip enhanced raman spectra of graphene," *Spectrochimica Acta Part A: Mol. Biomolecular Spectrosc.*, vol. 190, pp. 378–382, 2018.

[77] V. L. Loke, M. P. Mengüç, and T. A. Nieminen, "Discrete-dipole approximation with surface interaction: Computational toolbox for matlab," *J. Quantitative Spectrosc. Radiative Transfer*, vol. 112, no. 11, pp. 1711–1725, 2011.

[78] B. Schröder *et al.*, "Real-space imaging of nanotip plasmons using electron energy loss spectroscopy," *Phys. Rev. B*, vol. 92, no. 8, 2015, Art. no. 085411.

[79] F. G. De Abajo and A. Howie, "Retarded field calculation of electron energy loss in inhomogeneous dielectrics," *Phys. Rev. B*, vol. 65, no. 11, 2002, Art. no. 115418.

[80] J. Waxenegger, A. Trügler, and U. Hohenester, "Plasmonics simulations with the mnpbem toolbox: Consideration of substrates and layer structures," *Comput. Phys. Commun.*, vol. 193, pp. 138–150, 2015.

[81] P. Nagpal, N. C. Lindquist, S.-H. Oh, and D. J. Norris, "Ultrasmooth patterned metals for plasmonics and metamaterials," *Science*, vol. 325, no. 5940, pp. 594–597, 2009.

[82] H. Miranda, C. Rabelo, T. L. Vasconcelos, L. G. Cançado, and A. Jorio, "Study of the interaction between light and nanoantennas in tip-enhanced Raman spectroscopy," in *Proc. 4th Int. Symp. Instrum. Syst., Circuits Transducers*, 2019, pp. 1–5.
[83] C. Rabelo, H. Miranda, T. L. Vasconcelos, L. G. Cançado, and A. Jorio, "Tip-enhanced Raman spectroscopy of graphene," in *Proc. 4th Int. Symp. Instrum. Syst., Circuits Transducers*, 2019, pp. 1–6.
[84] H. Miranda, C. Rabelo, T. Vasconcelos, L. G. Cańcado, and A. Jorio, "Optical properties of plasmon-tunable tip pyramids for tip-enhanced Raman spectroscopy," *Physica Status Solidi - Rapid Res. Lett. Manuscript*, to be published, doi: 10.1002/pssr.202000212.

Thiago L. Vasconcelos received the M.Sc. and Ph.D. degrees in physics from the Federal university of Minas Gerais (UFMG), MG, Brazil. His doctoral thesis was on "Fabrication and study of probes for near-field optical microscopy". Since 2011, he is permanent employee at the National Institute of Metrology, Quality and Technology (Inmetro) - Brazil, where he has focused on TEM, EELS and FIB-lithography applied to nanofabrication of optical devices. In particular, he is the responsible for the TERS system at Inmetro, which he has implemented on 2014, and is the main inventor of the PTTP probes. His research interests include plasmonics, TERS, nanofabrication, TEM, EELS and materials metrology.

Bráulio S. Archanjo received the Ph.D. degree in physics from the Federal University of Minas Gerais, in Brazil in 2008 when he joined the National Institute of Metrology, Quality and Technology of Brazil (Inmetro) as a research scientist. In 2016, Dr. Archanjo has developed a postdoctoral project in 3D EELS tomography in plasmonic nanoantennas in cooperation with the Nacional Center for Electron Microscopy (NCEM) at Berkeley Labs. His research interest includes: graphene and other 2D materials, soil carbon, nanoparticles, transmission and scanning electron microscopy, focused ion beam, helium ion microscopy, scanning probe microscopy, Raman spectroscopy, X-ray photoelectron spectroscopy, and X-ray diffraction.

Bruno S. Oliveira received the B.Sc. degree in nanotechnology from the Universidade Federal do Rio de Janeiro (UFRJ) - Brazil, and the M.Sc. degree in metrology from the National Institute of Metrology, Quality and Technology (Inmetro) - Brazil, in 2016 and 2020, respectively. Since 2011, he was with Inmetro, where he focused on FIB-lithography for nanofabrication of optical devices. His research interests include SEM, FIB, and nanofabrication.

William F. Silva received the B.Sc in Nanotechnology from the Universidade Federal do Rio de Janeiro (UFRJ) – Brazil, in 2019. Since 2017, he was with Inmetro, where he focused on HIM nanopattern of graphene and TMDs samples.

Rafael S. Alencar is an Associated Professor at the Physics Department of the Federal university of Pará (UFPA), Brazil. He received the Ph.D. degree in physics in 2016 at the Federal university of Ceará with one-year research stay at the Université Claude Bernard Lyon 1 – Institut Lumière Matière (ILM), France, with emphasis on Raman spectroscopy under high pressure conditions on 1D and 2D systems. He spent two years (2016–2017 and 2018–2019) at the Federal university of Ceará as a Postdoctoral Fellow, working with high pressure Raman spectroscopy on 1D carbonaceous materials and one year (2017–2018) at the Federal university of Minas Gerais working with TERS applied on 2D systems.

Cassiano Rabelo received the Ph.D. in electrical engineering from the Federal university of Minas Gerais (UFMG), MG, Brazil. His doctoral thesis was on "Tip-enhanced Raman spectroscopy in graphene". Since 2013, he is an Associate Researcher at the Laboratory of Nanospectroscopy (LabNS), UFMG, with a focus on TERS.

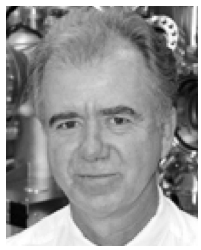

Carlos A. Achete received the Ph.D. degree in Metallurgical and Materials Engineering from the Federal University of Rio de Janeiro (1987). Retired Full Professor at the Alberto Luiz Coimbra Institute of Graduate Studies and Engineering Research (COPPE-UFRJ) where he headed the Thin Film and Surfaces Physics Area. Was Coordinator of the Metallurgy Undergraduate course. In 2003 he was assigned to Inmetro, where he was responsible for the creation of the Materials Metrology Division (Dimat). He is currently a Senior Researcher at Inmetro where he holds the position of Specialist in Metrology and Quality. Heads the ABNT Nanotechnology Committee. Has experience in Materials Engineering, Condensed Matter Physics, with an emphasis on physical and chemical properties of materials,thin films and Nanometrology

Ado Jorio is a Professor of Physics at the Federal University of Minas Gerais (UFMG). He received the doctoral degree from the same institution in 1999, followed by a postdoctoral fellowship at the Massachusetts Institute of Technology (MIT) (2000-2001). He was a Visiting Professor at ETH Zurich in 2013 and at FU Berlin in 2016. He held the positions of Coordinator of Strategic Studies and Information at Inmetro (2008-2009), and Director of Technological Transfer and Innovation (2010-2012), head of the Physics Department (2015-2016), and Dean of Research (2016-2018) at UFMG. His research focuses on development and applications of Raman spectroscopy to nanomaterials.

Luiz Gustavo Cançado is an Associated Professor at the Physics Department of the Federal University of Minas Gerais (UFMG), Brazil. He received the Ph.D. degree in 2006, at the same University, studying Raman spectroscopy of carbon nanostructures. He spent three years (2007–2009) at the Institute of Optics (University of Rochester), as a post-doctoral fellow in the Nano-optics group, and one year (2016) at CREOL, The College of Optics and Photonics (University of Central Florida), as a Visiting Professor in the Photonics Diagnostics of Random Media group. He is currently interested in near-field optics, with emphasis on tip-enhanced Raman spectroscopy applied to 2D materials. He also works on the metrology of mass-produced graphene.